

# Simulation Standard

Connecting TCAD To Tapeout

A Journal for Process and Device Engineers

## The Effect of Carrier Spilling on SRP Accuracy

### Introduction

Spreading Resistance Profiling (SRP) retains its popularity in the semiconductor industry by an inexpensive means of capturing dopant profile information. However, device engineers often incorporate SRP data into process simulation studies without properly considering SRP's many limitations. Failing to account for these limitations jeopardizes the reliability of the data and potentially lead designers to incorrect conclusions about a device.

This article briefly reviews the general concepts behind spreading resistance profiling and analyzes the impact of carrier spilling on both simulation studies and SRP accuracy. Finally, this article demonstrates how to reliably and accurately into a simulation study. The purpose of this article is not to discourage the use of SRP measurements, but rather to offer suggestions for using SRP measurements in order to obtain the most accurate results.

### SRP Measurements

Before proceeding to SRP's limits, it is necessary to revisit the concept of spreading resistance and how SRP data is collected. Spreading resistance (SR) is the resistance associated with a divergent current passing between electrodes on the surface of a semiconductor material. This quantity is determined by applying a known current between the electrodes on the surface of the sample and measuring the voltage drop between the probes. The spreading resistance value is calculated with Ohm's law. For a two probe system, the resistivity of the material is determined with the following expression, where  $a$  is an empirical quantity related to the effective electrical contact radius [1]:

$$\rho = 2R_{SR} \cdot a$$

Figure 1 is a simple two-probe spreading resistance measurement system. A structure's carrier concentration profile is measured by angle lapping the sample and making a series of SR measurements along the bevel. Profile depth is calculated as a function of the bevel angle. Correction factors are used to convert the spreading resistance values to carrier concentration levels. The technique of using spreading resistance to measure the thickness of diffused layers and impurity profiles was originally proposed by Mazur and Dickey [2] in 1966.

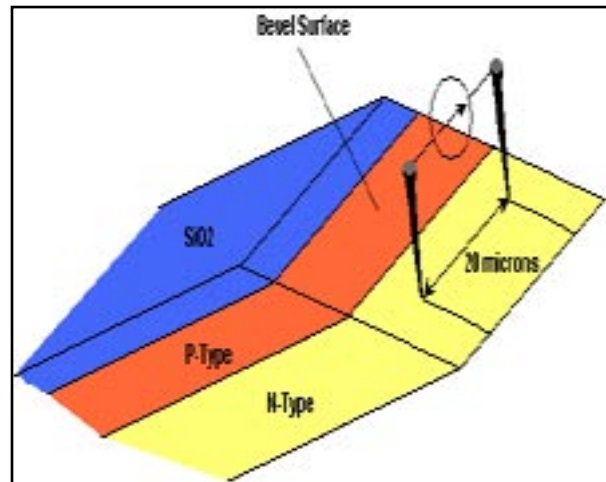


Figure 1. Schematic diagram of simple two-probe spreading resistance measurement system.

### Carrier Spilling

The total phenomena that affect SRP reliability are too numerous to describe here. This article focuses on carrier spilling, as it most directly impacts how SRP data is used within a simulation study.

Carrier spilling is a term that describes the diffusion of free carriers from a region of high concentration to a region of low concentration within a device structure. This is best understood by observing two blocks of equally-doped semiconductor as they are brought together. Figure 2 shows dopant and carrier concentrations within two

*Continued on page 2 ...*

### INSIDE

<i>Eye Diagram for a Direct Modulated Semiconductor Laser in ATLAS</i> .....	4
<i>Analysis of Light Power Dependence on the Leakage Current in a Buried Hetero- Structure p-InP Semiconductor Laser</i> .....	7
<i>Generating III-Nitride Transport Parameters with Silvaco Mocasim</i> .....	10
<i>Calendar of Events</i> .....	12
<i>Hints, Tips, and Solutions</i> .....	13

neighboring regions of uniformly-doped, N- and P-type silicon. Free carriers migrate across the PN junction from one region to another until the diffusion force is countered by the electric field created by the immobile dopant atoms.

How does carrier spilling affect the accuracy of SRP measurements? To answer this complicated question, we use a process simulation to obtain a better understanding of what is happening inside the structure. It is important to remember that SRP's measure the *carrier* concentration profile and not the actual dopant profile. The dopant profile at operating temperatures is immobile, the carrier profile is not. The very process of beveling the structure affects the boundary conditions of the system and alters the measured carrier concentration.

Figure 3a shows the net doping profile and total carrier profile for a simple gaussian PN junction. The total doping profile indicates a significant amount of carrier spilling in this structure. Carrier spilling from the P-region is dominant, and this places electrical junction (EJ) deeper in the structure than the metallurgical junction (MJ). Figure 3b shows the same profiles for the structure after moving down the bevel, resulting in the removal of 1.75 microns of silicon. Due to the higher concentration of holes, EJ remains deeper than MJ, but here a substantial portion of the free holes has also been removed. This reduces the effect of forward spilling and results in a slightly shallower (2.78 um vs 2.93 um) electrical junction depth. Continuing this analysis, Figures 3c and 3d show the structure after the removal of 1.8125 um and 1.875 um of silicon, respectively. Enough free holes have been removed from the structure in Figure 3c so that EJ is less than MJ, while in Figure 3d the concentration of electrons in the bulk of the structure overwhelms the remaining holes and eliminates the electrical junction altogether.

S.M Hu [3] originally identified the described carrier spilling effect. He performed an extensive study of the carrier spilling effects on SRP profiles and identified three situations in which carrier spilling could affect the electrical junction at the bevel. Figure 4 presents a diagram taken from [3] that shows the effects of carrier

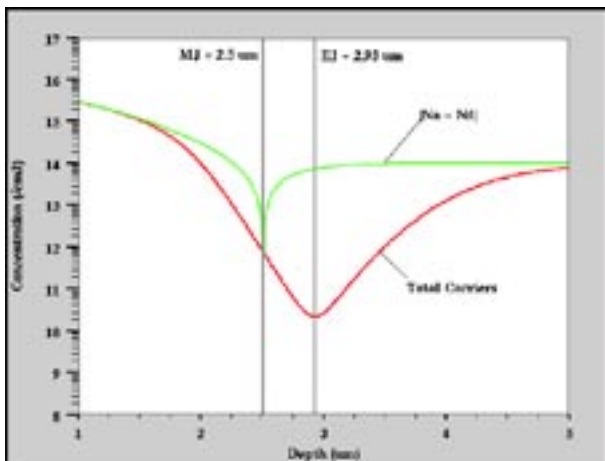


Figure 3a. Net doping and total carrier concentration profiles for simple gaussian PN junction.

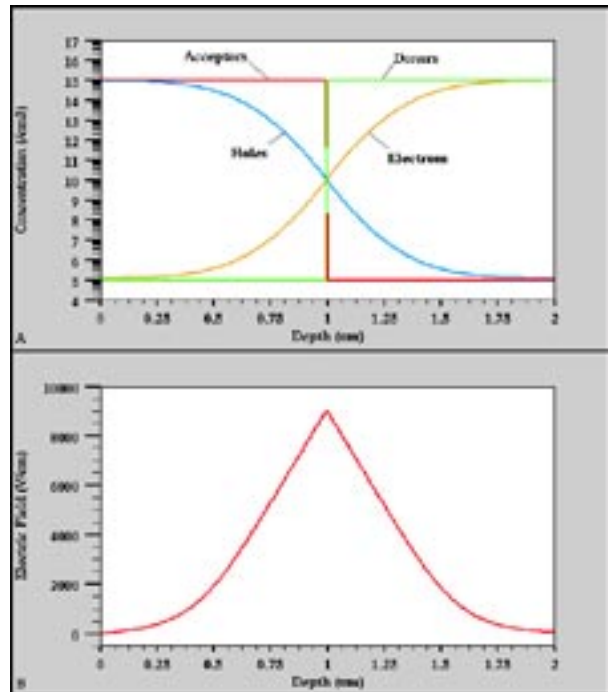


Figure 2. Dopant and carrier concentration profiles in neighboring p- and n-type silicon regions.

spilling on a beveled sample with a diffuse P-layer on a lightly doped N-type substrate. The electronic junction on the bevel is substantially different from that in the bulk. This is what the spreading resistance is supposed to measure. This diagram is a two dimensional view of the effects in Figures 3a-3d. Hu [3] later went on to study the effects of doping profile shapes, surface charge, and doping levels upon carrier spilling effects.

### Comparing Simulated Profiles to SRP Data

While the effect should not discourage the use of SRP measurements, it *must* be properly accounted for when comparing measured and simulated data. This effect prohibits the direct comparison of SRP data to the dopant profiles predicted by a process simulation package like

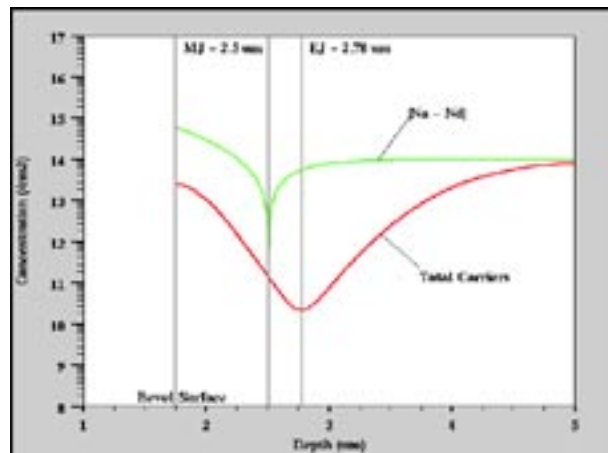


Figure 3b. Net doping and total carrier concentration profiles for simple gaussian PN junction after 1.75 microns of silicon has been removed.

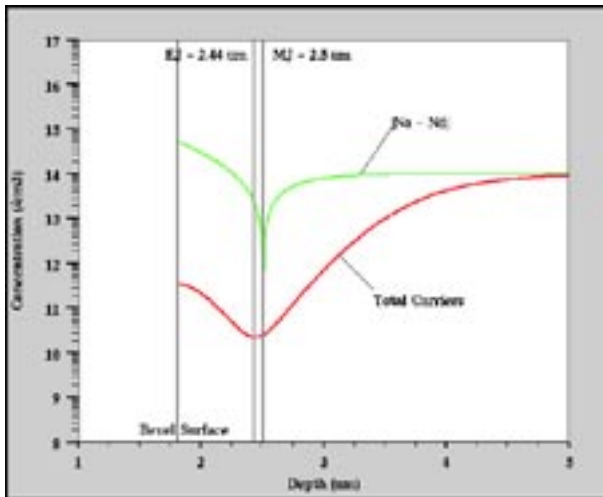


Figure 3c. Net doping and total carrier concentration profiles for simple gaussian PN junction after 1.8175 microns of silicon has been removed.

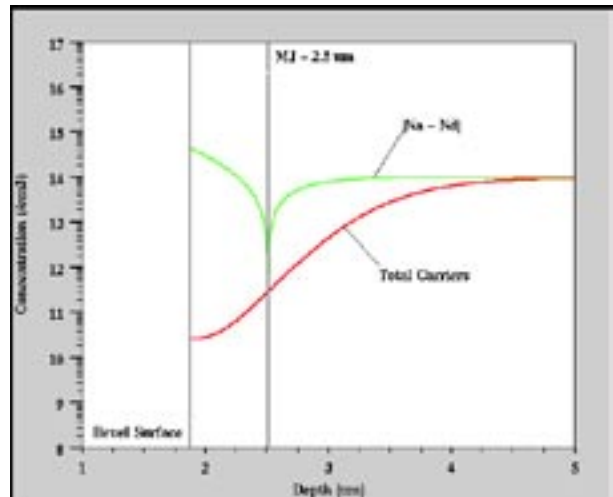


Figure 3d. Net doping and total carrier concentration profiles for simple gaussian PN junction after 1.875 microns of silicon has been removed.

Silvaco *ATHENA*. First, spreading resistance measures carrier concentration, not dopant concentration. Secondly, users must consider the removal of free carriers due to the beveling process. Silvaco has developed an extraction routine that automatically mimics the SRP process and generates an “SRP-like” carrier profile.

The correct syntax for extracting an SRP profile from a simulated structure is as follows:

```
extract name="SRP" curve(depth, srp
  material="silicon" mat.ocno=1\
  x.val=0.5) outfile="srp.dat"
```

A full description of the above syntax is found in Chapter 5 of the *VWF Interactive Tools User's Manual, Vol. 1*. It is also a predefined extraction routines that is available through *DeckBuilds'* Extraction menu. Figure 5 illustrate the effectiveness of the SRP extraction routine by comparing the spreading resistance profile predicted by *ATHENA* to actual SRP data taken from the source/drain region of an NMOS device. An excellent fit is achieved between the simulated and experimental SRP curves.

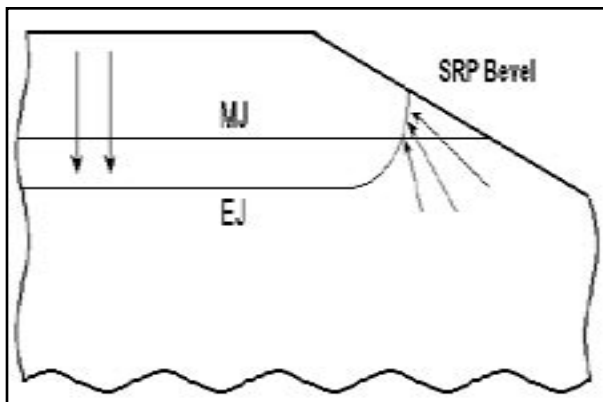


Figure 4. Two-dimensional cross section of beveled PN junction sample showing the qualitative effects of carrier spilling on a diffused p-layer in a lightly-doped n-type substrate.

## Summary

This article presented a brief review of spreading resistance profiling and discussed the effects of carrier spilling on the accuracy of SRP measurements. A full discussion of the all the phenomena affecting SRP measurements was not provided. It is *highly* recommended that any engineer who regularly incorporates SRP data into a simulation study reviews the work Hu [3] and others in an effort to better understand the strengths and weaknesses of the spreading resistance measurement process.

## References

- [1] S. Wolf and R.N. Tauber, *Silicon Processing for the VLSI Era Volume 1: Process Technology*, Lattice Press, Sunset Beach, CA (1986).
- [2] R.G. Mazur and P.H. Dickey, "A Spreading Resistance Technique for Resistivity Measurements on Silicon," *J. Electrochem. Soc.*, **113**, 255 (1996).
- [3] S.M. Hu, "Between Carrier Distributions and Dopant Atomic Distribution in Beveled Silicon Substrates," *J. Appl. Phys.*, **53**, 1499 (1982).

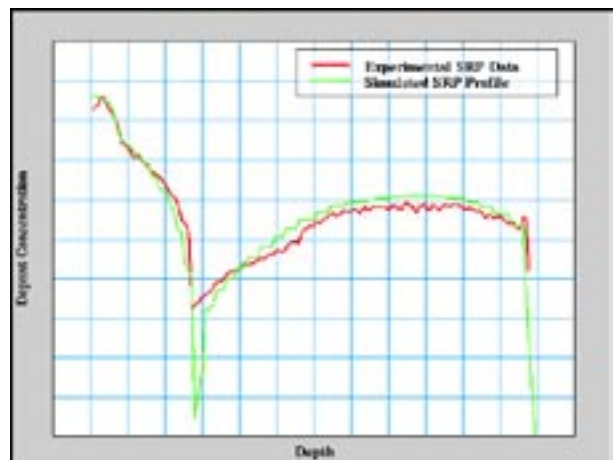


Figure 5. Comparison of simulated and measured SRP profiles for the source/drain region of a NMOS device.

# Eye Diagram for a Direct Modulated Semiconductor Laser in *ATLAS*

## Introduction

An eye diagram is a convenient way to visualise how the waveforms used to send multiple bits of data can potentially lead to errors in the interpretation of those bits. This is the so-called problem of intersymbol interference. An eye diagram is also a useful means for readily obtaining information regarding the timing jitter, voltage swing and transition time of the modulation data. The eye diagram operation in *ATLAS* is a post processing function where the eye diagram is created by taking the time domain signal and overlapping the traces for a certain number of symbols. The time domain signal in this article represents the output from a directly modulated semiconductor laser. The modulation of the laser drive current takes a pseudo-random form.

## LASER Simulation

Firstly a Fabry-Perot semiconductor laser is created in *ATLAS* using the advanced material module *Blaze*; the laser structure created is shown in Figure 1. The laser considered consists of an InGaAsP active region with InP cladding layers. An important parameter in a heterostructure device is bandgap alignment. How the bandgap difference is distributed between the conduction and valance bands has a large impact on the charge transport. In order to align the bandgaps use may be made of the ALIGN parameter in the MATERIAL statement. This specifies the fraction of the bandgap difference which will appear as the conduction band discontinuity. Internally, *Blaze* creates the desired conduction band

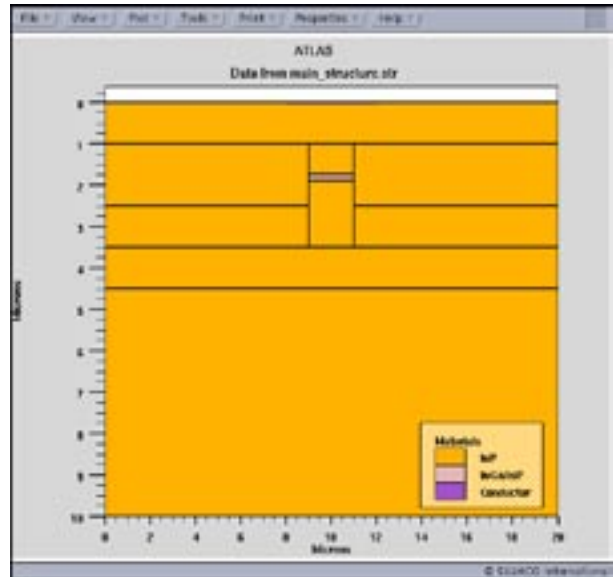


Figure 1. Cross sectional view of the simulated semiconductor laser device.

offset by modifying the electron affinity of the material for which the ALIGN parameter is specified. In this example ALIGN=0.6 has been used for the InP material, therefore 60% of the bandgap difference is assigned to the conduction band offset.

Semiconductor lasers are simulated in *ATLAS* with the module *Laser*. The module allows coupled electrical and optical simulation of semiconductor lasers. *Laser* works in conjunction with *Blaze* to solve the two dimensional Helmholtz equation in order to calculate the transverse optical field profile. It also allows calculation of the carrier recombination rate, optical gain and laser output power. The modal gain spectra for several longitudinal cavity modes is also readily available. Laser simulation is first initiated by specifying an independent rectangular mesh for the solution of the Helmholtz equation covering the entire active region. Since light may not entirely be contained within the active region this rectangular grid is chosen to extend so as to include an area slightly bigger than the active region. The turn on characteristics are shown in Figure 2 where it is clearly evident that for forward bias voltages from around 1.2V the output dramatically increases. Figure 3(a) shows the side view of the laser structure for a forward bias of 1.4V, where light emission is clearly evident, whilst Figure 3(b) shows the transverse mode profile obtained from Figure 3(a) by a 1 dimensional cut line across the active region. From figure 3(b) good optical confinement is evident.

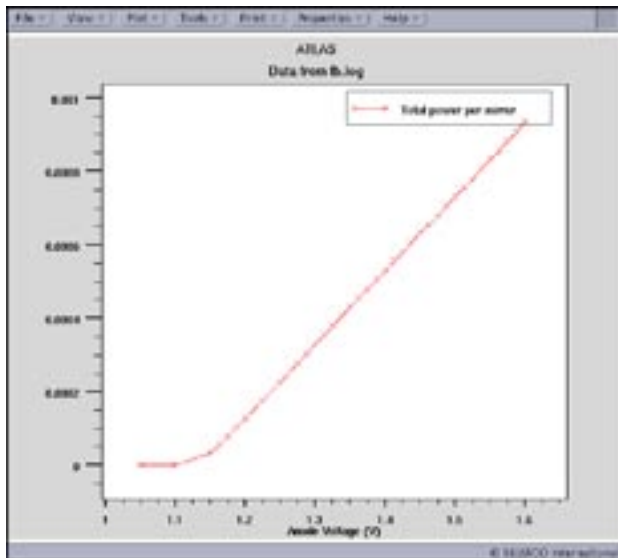


Figure 2. IV characteristic for simulated semiconductor laser.

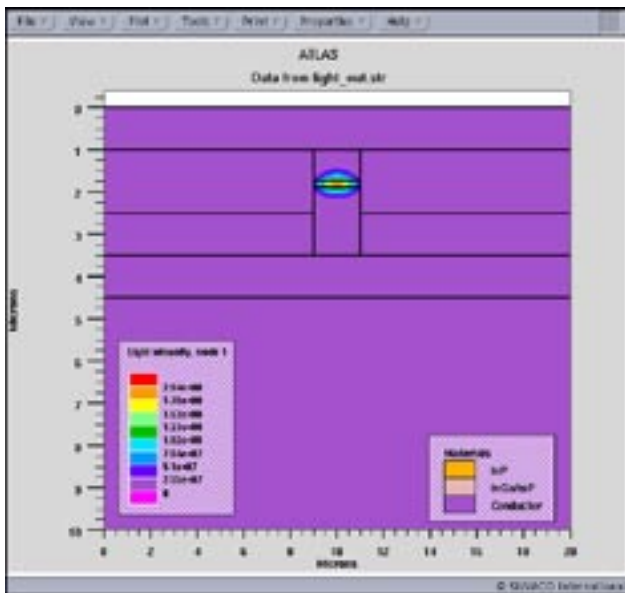


Figure 3(a). Cross sectional view showing optical intensity spatial properties.

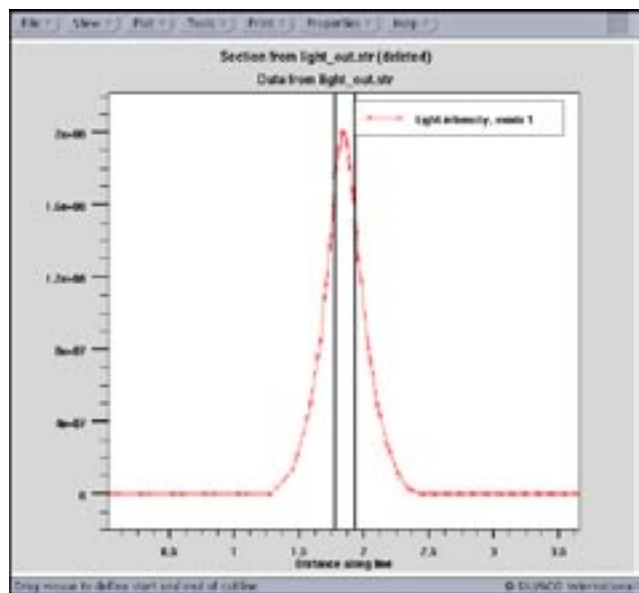


Figure 3(b). Light intensity profile obtained via a 1 dimensional cut-line through the centre of the semiconductor laser structure.

## Pseudorandom Modulation

Modulation of the laser is performed by adjusting the drive current. A forward bias of 1.3V is chosen to represent logic level 0, whilst a forward bias of 1.4V is chosen to represent logic level 1. These two logic levels are separately applied several times, the occurrence of a particular logic level being pseudorandom. In this way a pseudorandom modulation waveform, figure 4, is established. Example Atlas syntax for such a modulation scheme is detailed below.

```

solve vanode=$logic_1 ramptime=2e-10
  tstop=2.5e-9 dt=0.1e-11
solve vanode=$logic_0 ramptime=2e-10
  tstop=3.0e-9 dt=0.1e-11
solve vanode=$logic_0 ramptime=2e-10
  tstop=3.5e-9 dt=0.1e-11
solve vanode=$logic_0 ramptime=2e-10
  tstop=4.0e-9 dt=0.1e-11
solve vanode=$logic_1 ramptime=2e-10
  tstop=4.5e-9 dt=0.1e-11
solve vanode=$logic_0 ramptime=2e-10
  tstop=5.0e-9 dt=0.1e-11
solve vanode=$logic_0 ramptime=2e-10
  tstop=5.5e-9 dt=0.1e-11
solve vanode=$logic_1 ramptime=2e-10
  tstop=6.0e-9 dt=0.1e-11

```

Each statement in the above syntax represents a transient in *ATLAS*. Considering such a group of transient statements as that above, *ATLAS* solves for the first transient, where ramptime is the rise time of the pulse and tstop

is the time at which *ATLAS* stops the transient. For this first transient the pulse width is almost equal to tstop. On solving for the next transient in the group, risetime is once again the rise time of the pulse, however the duration of this pulse is essentially the difference between the tstop of the first transient and that of the second transient. *ATLAS* then proceeds onto the next transient and so on. In order to record the solution data for the transient simulations it is noted that a log file must be opened so that only transient data is recorded in it.

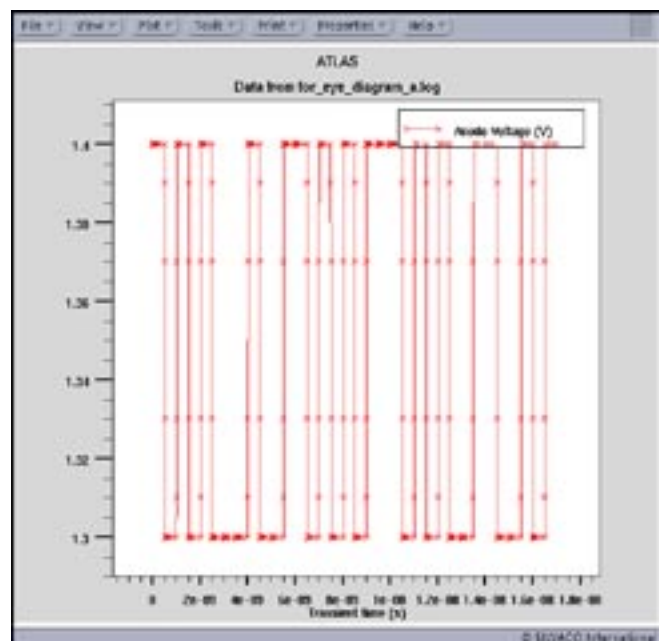


Figure 4. Anode voltage versus time for pseudorandom modulation scheme.

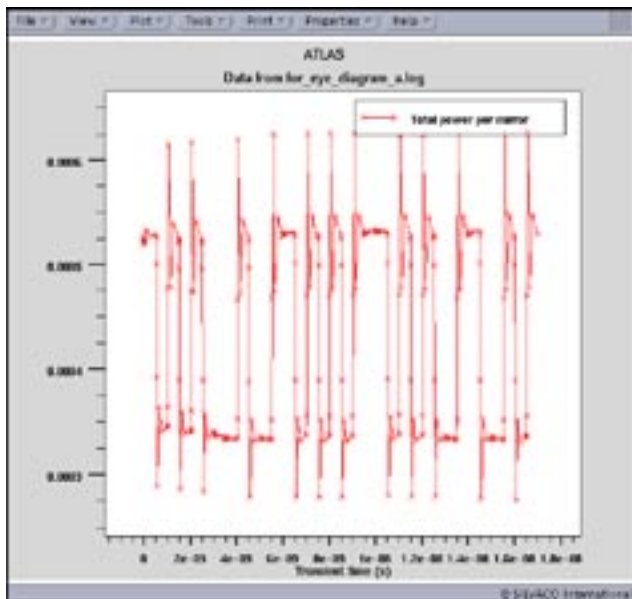


Figure 5. Light intensity output from the pseudorandom modulated semiconductor laser.

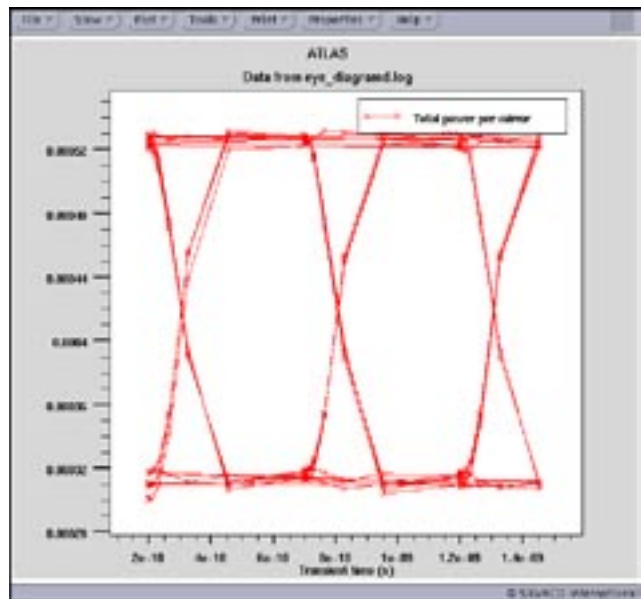


Figure 6. Eye diagram of the modulated output.

## Eye Diagram Creation

The output photon density versus time, Figure 5, shows the modulated output from the semiconductor laser. Another very useful representation of the modulation data in terms of examining inter symbol interference, timing jitter, voltage swing and transition time for example, is that of an eye diagram. The eye diagram is constructed by taking a large sample of the time domain signal and essentially splitting it up into several equal time segments, termed here as the period, which are then overlaid on each other. The *ATLAS* syntax used for this is detailed below:

```
eye.diagram inf=for_eye_diagram_a.log
outf=eye_diagramd.log t.start=1.0e-9
period=1.5e-9
```

In the above, `inf=for_eye_diagram_a.log` specifies the input log file that the eye diagram algorithm is to use i.e. the log file that the time domain information is stored in, `outf=eye_diagramd.log` is the output file that the eye diagram is to be stored in. The eye diagram algorithm requires the time at which the data in the input log file is to be used for the eye diagram, this is specified with `t.start`. The period i.e. time segment, that the eye diagram is to use is specified by `period`. Care must be taken to correctly chose this value. The resulting eye diagram is shown in Figure 6. As can be seen from the figure there is a large open eye in the figure indicative of a reasonable modulation scheme. Also of notice is that there exist a reasonable transition time, indicated by the slope of the walls of the eye diagram.

## Conclusion

It has been shown that a pseudo-random modulation scheme is easily performed in *ATLAS*. Also of ease is the creation of an eye diagram. Since it is a post processing function it is extremely quick to perform experiments regarding the choice of the period.

# Analysis of Light Power Dependence on the Leakage Current in a Buried Hetero- Structure p-InP Semiconductor Laser

## 1. Introduction

The buried heterostructure (BH) semiconductor laser finds favour in optical transmission systems due to its stable transverse mode property. Investigations into BH structure lasers have been performed [1] including use of a blocking current [2] in order to realize an optimized structure design. An effective device structure for reducing leakage current in BH laser diodes with semi-insulation doped Fe in InP blocking layers has been analyzed [3].

In this study, the leakage current and light output power as a function of the leakage current path is examined. The blocking region used follows p-n-p-n structure.

At the threshold current, the BH laser with a 0.3um leakage path, the quantum efficiency is over 20%. For higher injection currents, the leakage current increases and the light power will become saturated.

## 2. Device Structure

Since the BH laser examined in this article has a symmetrical structure, only the right hand side is simulated. Figure 1 shows a schematic cross-sectional view of the structure examined. This is the conventional BH laser structure; it consists of a p-n-p-n InP blocking layer by the side of the p- InGaAsP active region, giving a lasing wavelength of 1.55um. The cavity length is 250um, the thickness and width of the active InGaAsP region is 0.15um and 1um respectively. The reflectivity of the front and rear facets is 31%. To simulate the leakage path, two blocking layers are chosen to be variable whilst keeping the other blocking layers fixed. The thickness, delta t, is varied from from 0.1um to 0.5um.

## 3. Results and Discussions

To get the photon density during the current injection, *Laser* works in conjunction with *Blaze* to solve the two dimensional Helmholtz equation in order to calculate the transverse optical field profile. It also allows calculation of the carrier recombination rate, optical gain and laser output power. Poisson's equation, equation 1, and the electron and hole continuity equations, equations 2 and 3 respectively, are solved together with the photon rate equation. All of the terms in the equations detailed in this article are described in reference 4.

$$\text{div}(\epsilon \nabla \psi) = q(n - p - N_D^+ + N_A^-) + Q_T \quad (1)$$

$$\frac{\partial n}{\partial t} = \frac{1}{q} \text{div} \vec{J}_n - (R_{SRH} + R_{AUGER} + R_{sp} + R_{st}) \quad (2)$$

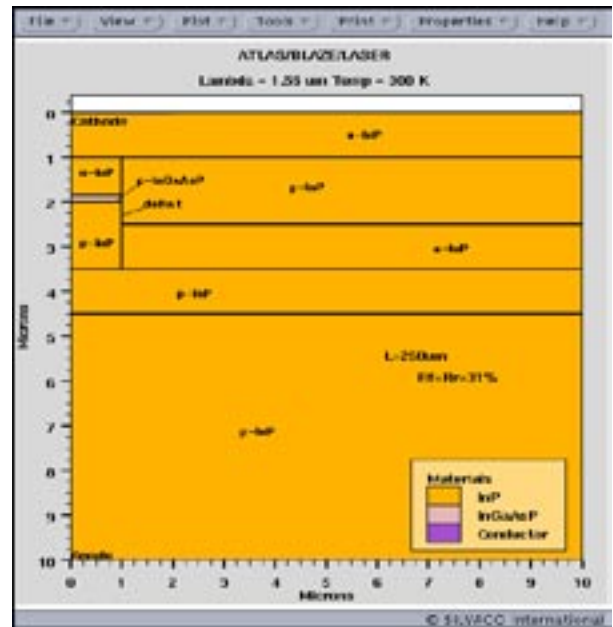


Figure 1. Schematic cross-sectional view of the half BH structure.

$$\frac{\partial p}{\partial t} = -\frac{1}{q} \text{div} \vec{J}_p - (R_{SRH} + R_{AUGER} + R_{sp} + R_{st}) \quad (3)$$

The recombination term of the carrier continuity equation includes the (non-radiative) SRH and Auger recombination rates, and the (radiative) spontaneous and stimulated recombination rates.

The optical gain of the laser links the electrical behaviour of the laser to the optical behaviour of the laser. The *Laser* module within *ATLAS* supports four gain models. The coupling between the stimulated carrier recombination rate ( $R_{st}$ ) and the photon density is given by equation 4.

$$R_{st}(x, y) = \sum \frac{c}{n_{eff}} g(x, y) |E(x, y)|^2 \cdot S \quad (4)$$

where  $E(x, y)$  is optical field distribution.

To determine the photon density  $S$ , *Laser* solves the photon rate equation [4], equation 5.

$$\frac{\partial S}{\partial t} = \left( \frac{c}{n_{eff}} G_m - \frac{1}{\tau_{ph}} \right) S + R_{sp} \quad (5)$$

$$\frac{1}{\tau_{ph}} = \frac{c}{n_{eff}} (\alpha_a + \alpha_f + \alpha_{mir}) \quad (6)$$

The photon lifetime, equation 6, is used to represent all of the losses in the laser [4].

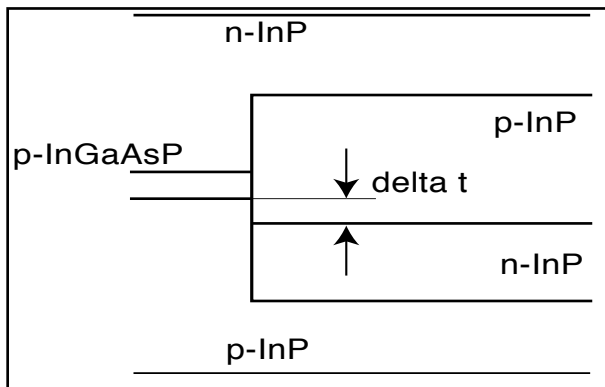


Figure 2. The leakage current path variable parameter.

In this study, the BH structure was chosen so that only the right hand side was modeled i.e. use was made of the symmetrical structure. The boundary condition was chosen so that at the top and bottom and along the right side of the structure the optical electric field is 0; the left side is set to mirror the boundary.

The recombination term was chosen to only consider the SRH, Auger and radiative recombination rate. The photon lifetime only considered the mirror losses. The free carrier loss and absorption loss were ignored.

The parameter of leakage current analysis of the BH laser is shown in Figure 2. The variable  $\delta t$  varies from 0.1 to 0.5 $\mu\text{m}$ . The active layer channel region was fixed at 2.5 $\mu\text{m}$ .

In Figure 3, the light output power as a function of anode current is shown for several  $\delta t$  values. The dark line is the point at which the efficiency is 22.6% at threshold

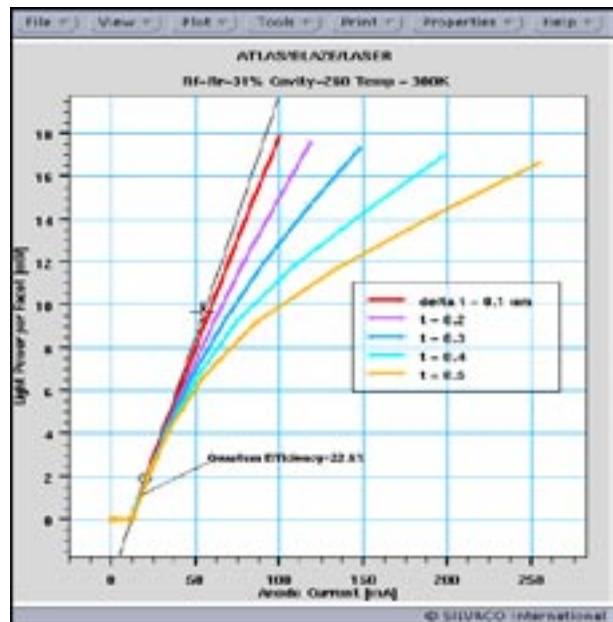


Figure 3. Light Power per Facet vs Anode Current characteristics.

current. For low injection currents i.e.  $< 20\text{mA}$ , all of the ratios of drive current to emitted light are the same. For injection currents  $> 20\text{mA}$ , the efficiency is to be low. The anode voltage and anode current characteristics are shown in figure 4. In this study the lasing threshold voltage is 1.15V. For voltages over 1.2V, the anode current is significantly dependent on the value  $\delta t$  takes. To investigate a value of 0.3 $\mu\text{m}$  for  $\delta t$  was chosen since this represents a common device value. Figures 5,6 and 7 show the energy band diagram for the active region and

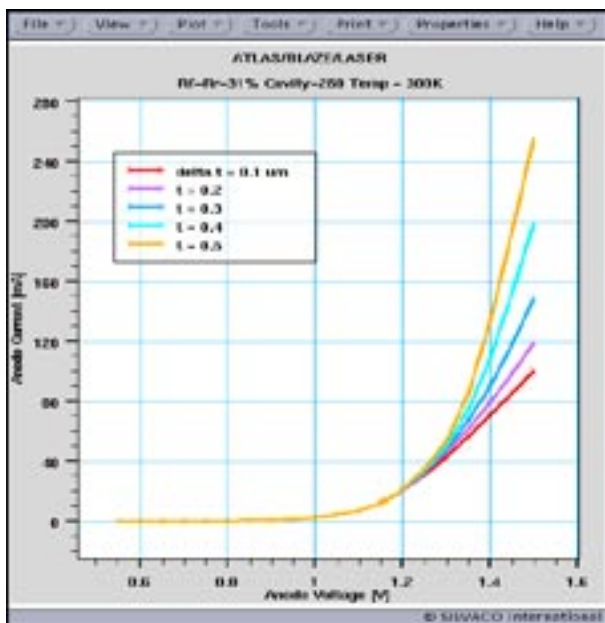


Figure 4. Anode Current- Anode Voltage Characteristics.

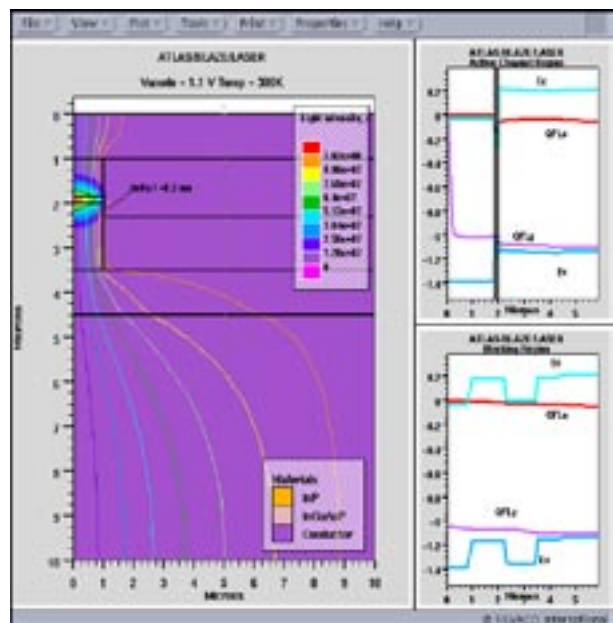


Figure 5. Current Flow distribution and Optical Field Energy Band diagram of the Active region and Blocking Region of the space 0.3 $\mu\text{m}$  at anode voltage of 1.1V.

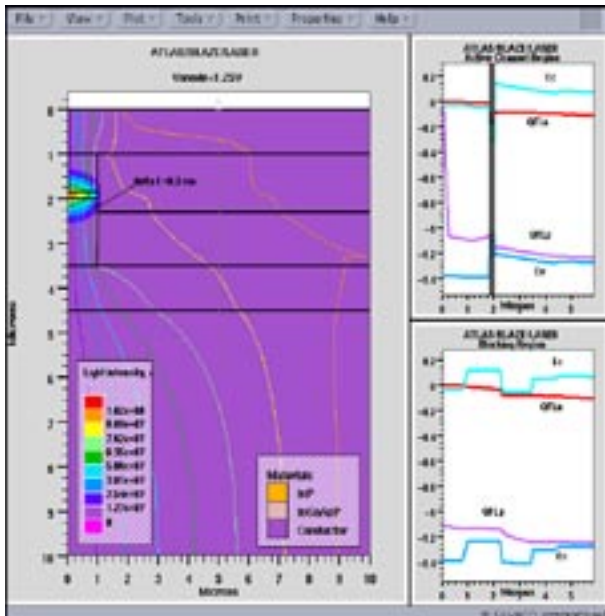


Figure 6. Current Flow distribution and Optical Field Energy Band diagram of the Active region and Blocking Region of the space 0.3um at anode voltage of 1.25V.

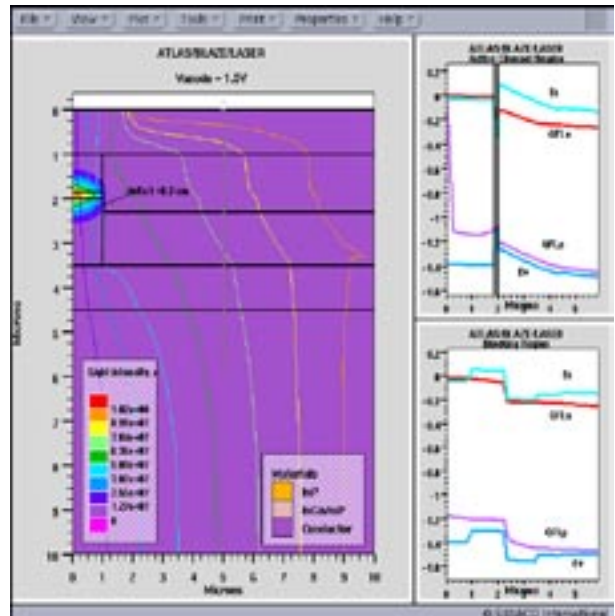


Figure 7. Current Flow distribution and Optical Field Energy Band diagram of the Active region and Blocking Region of the space 0.3um at anode voltage of 1.5V.

blocking region. In figure 5 at an anode voltage 1.1V, the current flow is seen to be through only the active region. In figure 6 at an anode voltage 1.25V, the current flow is observed to go through the blocking region. It is that the n-p-n-p blocking region was turn on to flow the current. For increased anode voltages, figure 7, it is seen that the current through the blocking region increases. The equivalent circuit in figure 8 shows the n-p-n-p thyristor device was combine the n-p-n transistor and p-n-p transistor. The active channel region is a p-i-n diode. The p-n-p collector and n-p-n base were shorted and connected to the anode of the p-i-n laser diode. When the leakage current flow to start to n-p-n base then, the n-p-n transistor will be turn on to flow the current it will be leakage current of the BH Laser.

#### 4. Summary

The leakage current of a BH laser has been investigated. The two layer changed to simulate the I- L characteristics. At the low injection condition, the slope efficiency is the same. When the anode voltage is over 1.2V, the leakage current was seen to depend on the leakage path distance as  $\Delta x$ .

#### References

- [1] N.K. Dutta, D.P. Wilt, and R.J.Nelson, J.Lightwave Technol. LT-2, 201 (1984)
- [2] S.Seki at al., Two-dimensional numerical analysis of current blocking mechanism in InP bur-ied heterostructure lasers J. Appl. Phys. 71(7), 1 April 1992 pp.3572-3578
- [3] S.Asada et al., Analysis of Leakage Current in Buried Heterostructure Lasers with Semiinsu-lationg Blocking Layers IEEE Journal of Quantum Electronics Vol. 25, No.6, JUNE 1989 pp.1362-1368
- [4] ATLAS Users Manual Vol.1

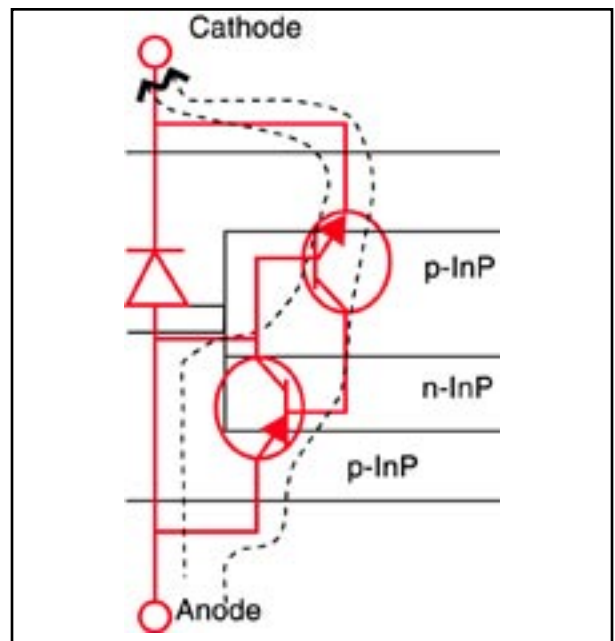


Figure 8. The equivalent circuit model for the active region and blocking region and the leak current path.

## Generation of III-Nitride Transport Parameters with *Mocasim*

*Mocasim* is an advanced three-valley Monte Carlo simulator designed to generate the transport parameters used in Silvaco's physical device simulators. It accurately calculates the material transport parameters of both direct and indirect band gap semiconductors, including group IV and III-V material systems. With the recent interest in III-Nitride material systems, we have added the capability of simulating materials with wurtzite as well as zincblende and diamond lattices. *Mocasim* derives a multi-dimensional parameter set, including mobility, velocity, energy and momentum relaxation times, and inter-valley potential energy, all of which can be extracted as a function of applied electric field, doping density, mole fraction(s), and lattice temperature.

*Mocasim* is a physically based simulator. As such, it has three major advantages over empirical modeling:

- It is predictive
- It provides insight
- It captures theoretical knowledge in a way that makes this knowledge easy to understand

Physically based simulation is different from empirical modeling. The goal of empirical modeling is to obtain analytic formula that approximate existing data with

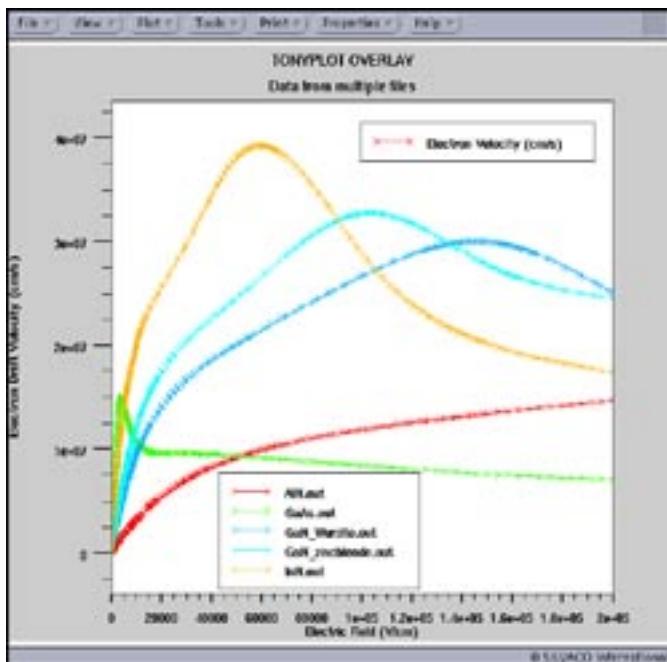


Figure 2. *Mocasim* generated curves of electron velocity versus electric field for GaAs, AnN, InN, wurtzite GaN and zincblende GaN.

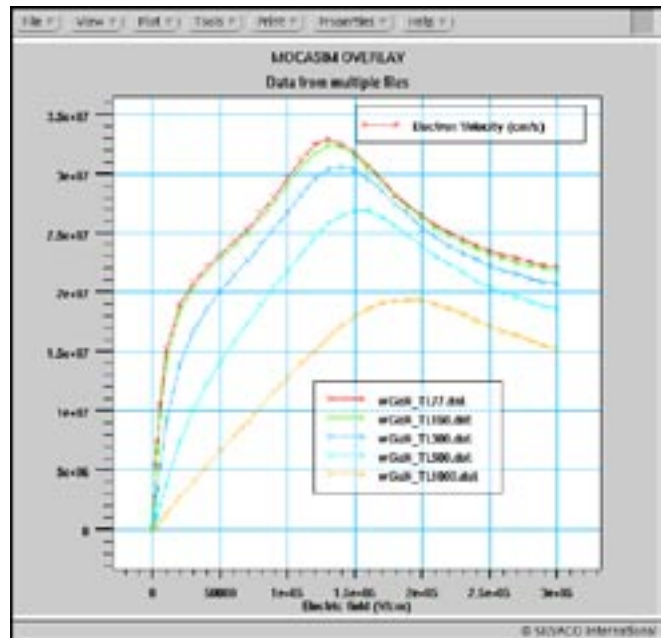


Figure 1. *Mocasim* generated curves of electron velocity versus electric field for wurtzite GaN at different ambient temperatures.

good accuracy and minimum complexity. Empirical models provide efficient approximation and interpolation. They do not provide insight, predictive capabilities, or encapsulation of theoretical knowledge. Physically based simulation is an alternative to experiments as a source of data. Empirical modeling can provide compact representations of data from either source.

Physically based simulation has become important for two reasons: First, it is almost always much quicker and cheaper than performing experiments. Second, it provides information that is difficult, or impossible to measure. These advantages are of special interest in the case of III-Nitride materials, which can be difficult to manufacture and measure.

There are drawbacks as well to physically based simulation. The drawbacks are that all the relevant physics must be incorporated into the simulator, and numerical procedures must be implemented to solve the associated equations. These tasks have been taken care of for users of *Mocasim*. Physical scattering mechanisms built into *Mocasim* include scattering from polar and non-polar optical phonons, deformation potential acoustic phonons, piezo-electric acoustic phonons, ionized or neutral impurity scattering, and inter-valley phonon scattering.

Parameter	z-GaN	w-GaN	w-AlN	w-InN
Lattice	Zincblende	Wurtzite	Wurtzite	Wurtzite
Density(g/cm <sup>3</sup> )	6.15	6.15	3.23	6.81
Longitudinal Speed of Sound (x1e5 cm/s)	4.57	6.56	9.06	6.24
Static Dielectric Constant	8.90	8.90	8.50	15.30
RF Dielectric Constant	5.35	5.35	4.77	8.40
Effective Masses				
Valley 0	0.150	0.190	0.480	0.110
Valley 1	0.400	0.400	1.000	1.000
Valley 2	0.600	0.600	1.000	1.000
Bandgap (eV)				
Valley 0	3.40	3.50	6.20	1.89
Valley 1	4.70	5.50	6.90	4.09
Valley 2	6.00	5.60	7.20	4.49
Non-Parabolicity (1/eV)				
Valley 0	0.213	0.183	0.044	0.419
Valley 1	0.065	0.065	0.000	0.000
Valley 2	0.029	0.029	0.000	0.000
Degeneracy				
Valley 0	1(G)	1(G)	1(G)	1(G)
Valley 1	3(X)	6(L-M)	6(L-M)	1(A)
Valley 2	4(L)	1(G')	2(K)	1(K)
Polar Optical Phonon Energy (meV)	91.20	91.20	99.20	89.00
Acoustic Deformation Potential (V)	8.30	8.30	9.50	7.10

Table 1. Basic set of material parameters used in the **Mocasin** velocity - field simulations for zincblende GaN and wurtzite GaN, AlN, and InN.

In the case of new materials, however, there is also the need to find the relevant parameters associated with these mechanisms. We have done a literature search 1-4 and assembled in Table 1. some of the needed parameters for wurtzite GaN, AlN, and InN, as well as zincblende GaN. This enables, through the appropriate interpolation routines, the parameters for ternary or quaternary materials from the binary parameters. Although there is not yet a consensus on precise values of these parameters, our simulations of electron velocity versus electric field with doping and temperature as parameters, as shown in Figure 1 and Figure 2, have been compared with measurements and other (non-commercial) simulations found in the literature with consistent results. Our Figure 1 can be compared with Bhapkar's Figure 1a for electron velocity vs field for wurtzite GaN with  $N_d=1e17$  cm<sup>-3</sup> for a range of temperatures: T=77, 150, 300, 500, and 1000K. Our Figure 2 shows electron velocity vs field for GaAs, InN, AlN, and GaN in both zincblend and wurtzite forms. Compare with Faramond5 for wurtzite GaN, InN, and AlN; Figure 2 in Kolnik4 for wurtzite and zincblende GaN; and Foutz3 for GaAs and GaN.

## References

1. Michael Shur's website: //nina.ecse.rpi.edu/shur/GaN.html
2. U. D. Bhapkar, M. S. Shur, J. Appl. Phys. 82, 1649 (1997).
3. B. E. Foutz, et al., Appl. Phys. Lett. 70, 2849 (1997).
4. J. Kolnik, et al., J. Appl. Phys. 78, 1033 (1995).
5. M. Farahmand, et al., IEEE Trans. Elect. Dev. 48, 535 (2001).

# Calendar of Events

## August

1
2
3
4
5
6
7
8
9
10
11
12
13
14
15
16
17
18
19
20
21
22
23
24
25 ISLPED - Soeul, Korea ISCS - San Diego, CA
26 ISLPED - Soeul, Korea ISCS - San Diego, CA
27 ISLPED - Soeul, Korea ISCS - San Diego, CA
28
29
30
31

## September

1
2
3 SISPAD - Cambridge, MA
4 SISPAD - Cambridge, MA
5 SISPAD - Cambridge, MA
6 EGAOSAS - Munich, Germany
7 EGAOSAS - Munich, Germany
8
9 GaSa IC Symposium-San Diego
10 GaSa IC Symposium-San Diego
11 GaSa IC Symposium-San Diego
12 GaSa IC Symposium-San Diego
13
14 BCTM - Toulouse, France
15 BCTM - Toulouse, France RADECS - Netherlands
16 BCTM - Toulouse, France RADECS - Netherlands SSDM - Tokyo, Japan ESSDERC - Portugal
17 SSDM - Tokyo, Japan ESSDERC - Portugal
18 SSDM - Tokyo, Japan ESSDERC - Portugal
19 SSDM - Tokyo, Japan
20
21 CICC - San Jose, CA
22 CICC - San Jose, CA
23 CICC - San Jose, CA
24 CICC - San Jose, CA
25
26
27
28
29 IEEE SOI-Newport Beach, CA
30 IEEE SOI-Newport Beach, CA CMRF - Toulouse, France

## Bulletin Board



### PolarFab Delivers Silvaco Process Design Kits for Power Device Process

PolarFab, a U.S.-based pure-play semiconductor foundry and Silvaco announced the availability of process design kits (PDKs) for PolarFab's BP30 30V complementary bipolar process supporting Silvaco circuit simulation and custom IC CAD tools.

The kit, which includes SmartSpice™ models, Scholar™ schematic symbols, Guardian™ DRC and LVS rule decks, and parameterized cells for the PolarFab BP30 bipolar process, is available from PolarFab.



### Silvaco Donates \$2.4M of EDA Software to University of Washington

Silvaco donated \$2.4 million of software to the University of Washington College of Engineering to create a intellectual hub for advanced technology computer aided design (TCAD) research and development.

The college of engineering faculty and graduate students will use this software to model reliability and performance of semiconductors as part of a joint development project between the University and Silvaco.

If you would like more information or to register for one of our workshops, please check our web site at <http://www.silvaco.com>

The Simulation Standard, circulation 18,000 Vol. 13, No. 8, August 2003 is copyrighted by Silvaco International. If you, or someone you know wants a subscription to this free publication, please call (408) 567-1000 (USA), (44) (1483) 401-800 (UK), (81)(45) 820-3000 (Japan), or your nearest Silvaco distributor.

The following trademarks and service marks are the property of Silvaco International. Registered Marks:® Virtual Wafer Fab, Silvaco. Trademarks:™ Simulation Standard, ATHENA, Analog Alliance, Legacy, Manufacturing Tools, Automation Tools, SFLM, VICTORY, Ranger3D Nomad, VYPER, SmartSpice, PSTATS, UTMOST IV, Measure, DISCOVERY, MERCURY, Optolith, TCAD Driven CAD, TonyPlot3D, RESILIENCE, Flash, ATHENA Interpreter, Interactive Tools, DeckBuild, DevEdit, ANALOG EXPRESS, CELEBRITY, SSuprem3, ATLAS, ATLAS Interpreter, Luminous2D/3D, MC Implant, S-Pisces, TonyPlot, FastLargeSignal, SmartStats, Ferro, DevEdit3D, Interpreter, Quantum2D/3D, SDDL, Circuit Optimizer, MaskViews, TFT2D/3D, Radiant, SSuprem4, Elite, FastBlaze, Mocasim, Silicides, MC Depo/Etch, FastNoise, Clarity, Blaze/Blaze3D, Device3D, Frontier, TwinSim, MixedMode2D/3D, VCSELS, Maverick, Envoy, Giga2D/3D, FastGiga, Guardian, Scout, FastMixedMode, Laser, Dragon, Expert, Spirit, Beacon, Savage, Harm, Zenith, Vision, Scholar, SN, UTMOST, UTMOST II, UTMOST III, UTMOST IV, PROMOST, SPAYN, ExpertViews, UTMOST IV Fit, FastSpice, Twister, Blast, MixSim, SmartLib, TestChip, Promost-Rel, RelStats, RelLib, Ranger, LISA, QUEST, EXACT, CLEVER, STELLAR, HIPEX-RCR, HIPEX-Net, HIPEX-RC, Connecting TCAD to Tapeout, and UTMOST IV Spice Modeling. All other product or company names are trademarks of their respective owners.

# Hints, Tips and Solutions

William French Ph.D., Applications and Support Manager

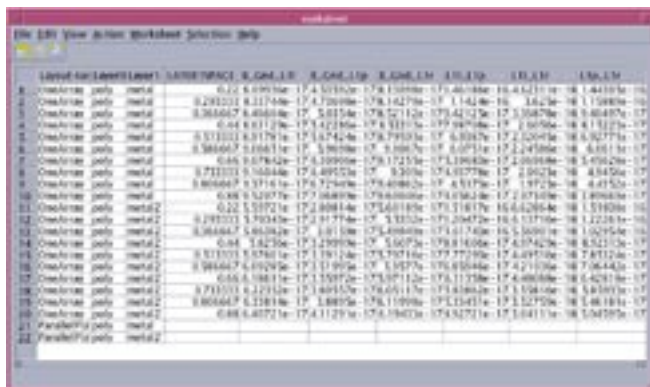
**Q. EXACT has powerful scripting utilities for manipulating the final capacitance data and variables but is there an easier graphical front end that would also allow me to view the data ?**

A. Recent improvements to *EXACT* have included the addition of the Worksheet utility. When an experiment has been completed within *EXACT* the Worksheet may be accessed from the "View->Data" pulldown menu of the main *EXACT* window shown in Figure 1. All the data from the experiment, including selected layers, process variables, layout variables and extracted capacitance data, will be sent to the Worksheet. An example of this is shown in Figure 2 where columns are shown for the test structure name, the chosen process layer names, the layout parameter that has been varied and finally the calculated capacitance values from *EXACT*.

The worksheet allows a number of operations to be performed which include;

- column/row selection
- inter-column or inter-row calculations into new columns or rows respectively
- selection of data for plotting in *TonyPlot*
- selection of data that can then be sent to *SPAYN* for statistical analysis
- equation fitting through the use of the Silvaco Optimiser

The Worksheet allows a graphical approach to viewing the variables and data that otherwise would be accessed only through the *EXACT* script utilities. As an example of this we can select certain data, as shown in Figure 3, which we wish to view. Once selected the Worksheet pulldown menu option "Selection->Tonyplot" will then



Layer	LAYERSPACE	B_GND_L1	B_GND_L1p	B_GND_L1r	L1L_L1p	L1L_L1r	L1p_L1r
1	0.2	5.0975e-17	1.4521e-16	1.1009e-16	1.4211e-16	1.4410e-16	1.4410e-16
2	0.2	2.2022e-16	8.2117e-16	1.4700e-16	1.8142e-16	1.8142e-16	1.8142e-16
3	0.2	3.2650e-17	4.6440e-16	1.7057e-16	1.7852e-16	1.7942e-16	1.7942e-16
4	0.4	6.8112e-16	1.7142e-16	1.9331e-16	1.9399e-16	1.9399e-16	1.9399e-16
5	0.2	5.5122e-16	1.0179e-16	1.5174e-16	1.5993e-16	1.5993e-16	1.5993e-16
6	0.2	5.5846e-17	1.0361e-16	1.5388e-16	1.6207e-16	1.6207e-16	1.6207e-16
7	0.4	5.0784e-16	1.5399e-16	1.7125e-16	1.7193e-16	1.7193e-16	1.7193e-16
8	0.2	5.7122e-16	1.0444e-16	1.5495e-16	1.6305e-16	1.6305e-16	1.6305e-16
9	0.2	5.8666e-17	1.0716e-16	1.5749e-16	1.6524e-16	1.6524e-16	1.6524e-16
10	0.4	6.1222e-16	1.7104e-16	1.9384e-16	1.9452e-16	1.9452e-16	1.9452e-16
11	0.2	5.2072e-16	1.7188e-16	1.7161e-16	1.7161e-16	1.7161e-16	1.7161e-16
12	0.2	5.2072e-16	1.7188e-16	1.7161e-16	1.7161e-16	1.7161e-16	1.7161e-16
13	0.2	5.2072e-16	1.7188e-16	1.7161e-16	1.7161e-16	1.7161e-16	1.7161e-16
14	0.4	5.1422e-16	1.7101e-16	1.9384e-16	1.9452e-16	1.9452e-16	1.9452e-16
15	0.2	5.5122e-16	1.0179e-16	1.5174e-16	1.5993e-16	1.5993e-16	1.5993e-16
16	0.2	5.5122e-16	1.0179e-16	1.5174e-16	1.5993e-16	1.5993e-16	1.5993e-16
17	0.2	5.5122e-16	1.0179e-16	1.5174e-16	1.5993e-16	1.5993e-16	1.5993e-16
18	0.2	5.5122e-16	1.0179e-16	1.5174e-16	1.5993e-16	1.5993e-16	1.5993e-16
19	0.2	5.5122e-16	1.0179e-16	1.5174e-16	1.5993e-16	1.5993e-16	1.5993e-16
20	0.2	5.5122e-16	1.0179e-16	1.5174e-16	1.5993e-16	1.5993e-16	1.5993e-16
21	0.2	5.5122e-16	1.0179e-16	1.5174e-16	1.5993e-16	1.5993e-16	1.5993e-16
22	0.4	6.4072e-16	1.7112e-16	1.9384e-16	1.9452e-16	1.9452e-16	1.9452e-16

Figure 2. The *EXACT* Worksheet showing the data from the experiment.



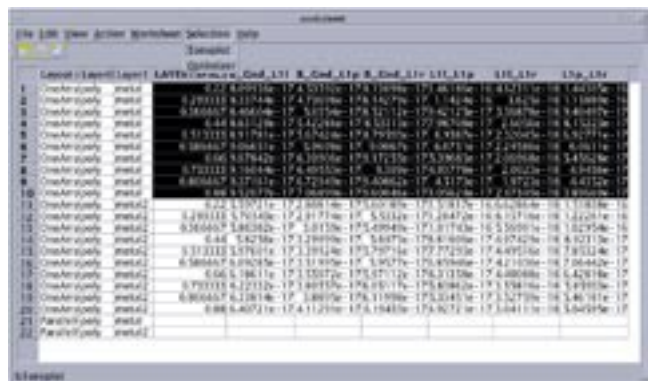
Figure 1. Once the *EXACT* experiment has been run the data may be accessed through the Worksheet.

send this data to *TonyPlot*. Figure 4 shows the selected data from Figure 3 where the measured capacitance values (B\_Gnd\_L1l, B\_Gnd\_L1p, B\_Gnd\_L1r, L1L\_L1p, L1L\_L1r and L1p\_L1r) have been plotted against the layout variable LAYER1SPACE.

Many other features are available through this Worksheet which shall be described in future publications.

**Q. EXACT allows the measured data to be fitted to polynomial expressions using the scripting utilities. Is there a way to instead optimise the fitting interactively ?**

A. Figure 5 shows a script which performs an interactive optimization. A detailed description of the syntax in this script is available in the *EXACT User's Manual*. In step 1



The screenshot shows the EXACT Worksheet with a selection of data highlighted in black. The columns are the same as in Figure 2. The selection covers rows 1 through 22, with columns 2 through 8 highlighted.

Figure 3. Selection of data in the Worksheet to be sent to *TonyPlot*.

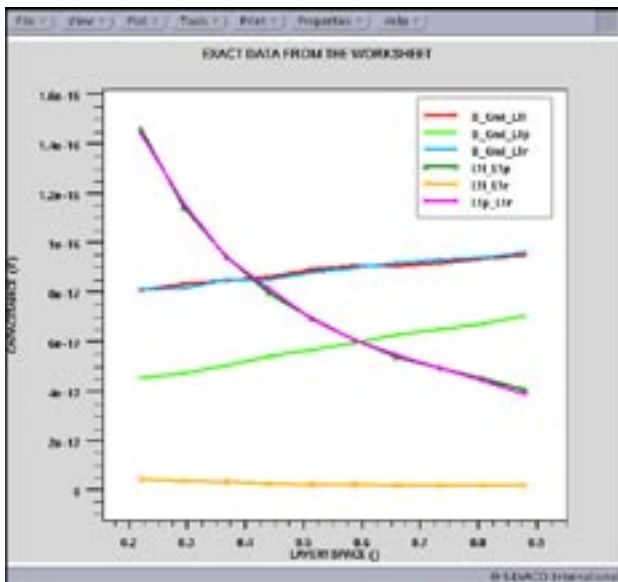


Figure 4. Data from the Worksheet plotted within **TonyPlot**.

```

1.1. select the data that we want to use
do = DatabaseLoad("optimizer_db")

extract_name("Carea", "C_Gnd", "Plate");
extract_name("Ccap1", "C1p", "L1");
extract_name("Ccap", "C_Gnd", "L1");

!extract.combinations = 0;
!poly.combinations = 0;

! table for parallel plate for all other combinations
table = select(do, "ParallelPlate", poly.combinations, {"Width",
["Carea"];
save_table(table, do, "table1.csv");
save_table(table, TOWPOINT, "table1.txt");

! table 2 for overlap for all other layers combination
table2 = select(do, "Overlap", poly.combinations, {"Layer",
"LayerWidth"}, {"Ccap1", "C_Gnd");

! scale data to FF
! multiply capacitance values by 1e15
column_scalar(table1, "Carea", "FF", 1e15);
column_scalar(table2, "Ccap1", "FF", 1e15);
column_scalar(table2, "C_Gnd", "FF", 1e15);

1.2. Define the model for optimisation
equation = "Ccap1*(2*W*(L1 - W)/2) + C_Gnd*(L1*W) /
(L1*W*(SPACE) + W*(SPACE) + W*(SPACE) + W*(SPACE) + W*(SPACE)";

1.3. Bring up Optimiser GUI and perform interactive optimisation
opt_gui = Optimize_Fit(workspace) (table1) (table2) (poly.combinations)
("OPT_GUI") "GUI";

! Save Results
save_table(opt_gui.results, do, "res_opt_gui.csv");
save_table(table1, do, "table1.csv");
save_table(table2, TOWPOINT, "table2.txt");

```

Figure 5. **EXACT** script for performing the analysis on the experiment data.

in the script the capacitance database is loaded and various selections are made that result in a table of variables and data that we wish to work with, which in this case is the NEARBODY capacitance (which is the capacitance effect between two conductors edge-to-edge). The capacitance data from **EXACT** is in the units of Farads but for the purposes of fitting the script scales these values into units of femtoFarads. In step 2 we define an equation that will be used to fit the data to and in step 3 we force the optimiser to come up in interactive mode.

Figure 6 shows the Optimiser window that appears within which the user can modify the equation, set up the optimization Control parameters and view the results of the optimisation. In this case we show the variations of the equation coefficients (N0, N1, N2, N3, N4, N5) during the optimisation iterations.

When the optimisation has finished the original data from **EXACT** and the fitted equation, with the optimised parameters, may be plotted in **TonyPlot**. As shown in Figure 7 an excellent fit is obtained.

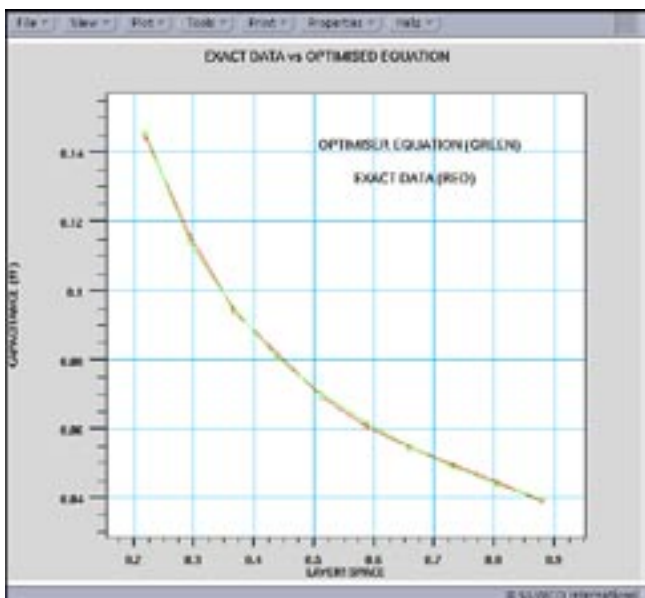


Figure 7. Comparison of the original EXACT capacitance data and the equation used to fit the data which has the optimised coefficients.

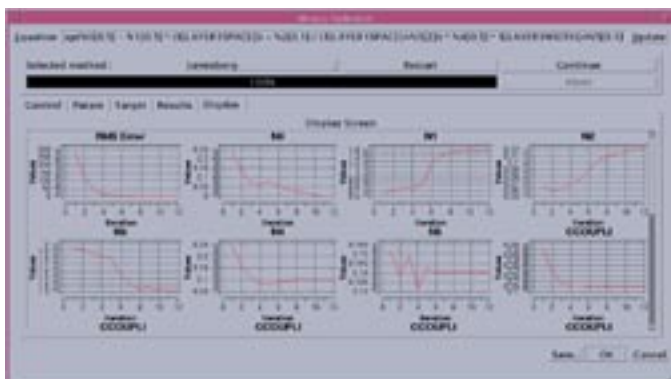


Figure 6. The **Optimizer** window that allows interactive control of the fitting process.

*Acknowledgments to Eric Guichard and his team for this Hints and Tips.*

**Call for Questions**

If you have hints, tips, solutions or questions to contribute, please contact our Applications and Support Department  
 Phone: (408) 567-1000 Fax: (408) 496-6080  
 e-mail: support@silvaco.com

**Hints, Tips and Solutions Archive**

Check our our Web Page to see more details of this example plus an archive of previous Hints, Tips, and Solutions  
[www.silvaco.com](http://www.silvaco.com)

## Join the Winning Team!

- PROCESS AND DEVICE APPLICATION ENGINEERS
- SPICE APPLICATIONS ENGINEERS
- CAD APPLICATIONS ENGINEERS
- SOFTWARE DEVELOPERS

EMAIL TO: [CAREERS@SILVACO.COM](mailto:CAREERS@SILVACO.COM)



# SILVACO

## INTERNATIONAL

### USA Headquarters:

**Silvaco International**  
4701 Patrick Henry Drive, Bldg. 2  
Santa Clara, CA 95054 USA

Phone: 408-567-1000  
Fax: 408-496-6080

[sales@silvaco.com](mailto:sales@silvaco.com)  
[www.silvaco.com](http://www.silvaco.com)

### Contacts:

**Silvaco Japan**  
[jpsales@silvaco.com](mailto:jpsales@silvaco.com)

**Silvaco Korea**  
[krsales@silvaco.com](mailto:krsales@silvaco.com)

**Silvaco Taiwan**  
[twsales@silvaco.com](mailto:twsales@silvaco.com)

**Silvaco Singapore**  
[sgsales@silvaco.com](mailto:sgsales@silvaco.com)

**Silvaco UK**  
[uksales@silvaco.com](mailto:uksales@silvaco.com)

**Silvaco France**  
[frsales@silvaco.com](mailto:frsales@silvaco.com)

**Silvaco Germany**  
[desales@silvaco.com](mailto:desales@silvaco.com)

*Products Licensed through Silvaco or e\*ECAD*

